

# Triple-junction solar cells with cyanate in ultrawide-bandgap perovskites

<https://doi.org/10.1038/s41586-024-07226-1>

Received: 10 September 2023

Accepted: 22 February 2024

Published online: 4 March 2024

 Check for updates

Shunchang Liu<sup>1,2,7</sup>, Yue Lu<sup>3,7</sup>, Cao Yu<sup>4</sup>, Jia Li<sup>2</sup>, Ran Luo<sup>1,2</sup>, Renjun Guo<sup>2</sup>, Haoming Liang<sup>1,2</sup>, Xiangkun Jia<sup>1,2</sup>, Xiao Guo<sup>1,2</sup>, Yu-Duan Wang<sup>1,2</sup>, Qilin Zhou<sup>1,2</sup>, Xi Wang<sup>1,2</sup>, Shaofei Yang<sup>4</sup>, Manling Sui<sup>3</sup>, Peter Müller-Buschbaum<sup>5,6</sup> & Yi Hou<sup>1,2</sup>✉

Perovskite bandgap tuning without quality loss makes perovskites unique among solar absorbers, offering promising avenues for tandem solar cells<sup>1,2</sup>. However, minimizing the voltage loss when their bandgap is increased to above 1.90 eV for triple-junction tandem use is challenging<sup>3–5</sup>. Here we present a previously unknown pseudohalide, cyanate ( $\text{OCN}^-$ ), with a comparable effective ionic radius (1.97 Å) to bromide (1.95 Å) as a bromide substitute. Electron microscopy and X-ray scattering confirm OCN incorporation into the perovskite lattice. This contributes to notable lattice distortion, ranging from 90.5° to 96.6°, a uniform iodide–bromide distribution and consistent microstrain. Owing to these effects, OCN-based perovskite exhibits enhanced defect formation energy and substantially decreased non-radiative recombination. We achieved an inverted perovskite (1.93 eV) single-junction device with an open-circuit voltage ( $V_{\text{oc}}$ ) of 1.422 V, a  $V_{\text{oc}} \times \text{FF}$  (fill factor) product exceeding 80% of the Shockley–Queisser limit and stable performance under maximum power point tracking, culminating in a 27.62% efficiency (27.10% certified efficiency) perovskite–perovskite–silicon triple-junction solar cell with 1 cm<sup>2</sup> aperture area.

Perovskite-based tandem solar cells offer an effective approach for surpassing the Shockley–Queisser efficiency limits in existing photovoltaic technologies, including silicon, copper indium gallium selenide and organic photovoltaics<sup>6,7</sup>. The advancement of 1.67 eV and 1.77 eV wide-bandgap perovskites has catalysed rapid progress in the field of perovskite-based dual-junction solar cells<sup>8–11</sup>. With a current power conversion efficiency (PCE) record of 33.7% for perovskite/Si tandem, these cells have even exceeded the performance of their best dual-junction III–V semiconductor counterparts (32.9%) (ref. 12).

Drawing inspiration from III–V multijunction solar cells, the incorporation of an ultrawide-bandgap (UWBG) perovskite with a bandgap above 1.90 eV into a triple-junction solar cell (TJSC) offers a pathway for further boosting the efficiency, potentially achieving efficiencies as high as 51% (ref. 13). Initial studies have indicated the feasibility of constructing perovskite-based TJSCs, with efficiencies reaching 24.3% in all-perovskite configurations and 22.23% in perovskite/perovskite/Si configurations<sup>14,15</sup>.

The bandgaps of perovskites largely depend on the orbital couplings between lead (Pb) and halogens (represented by X)<sup>16</sup>. Adjusting the mixture of iodine (I) and bromine (Br) is the most practical way to modify the bandgap, which increases as the proportion of Br increases. However, normally, when the Br fraction exceeds 20%, the material exhibits increased non-radiative recombination and phase segregation on illumination, which leads to reduced open-circuit voltage ( $V_{\text{oc}}$ ) and instability during device operation<sup>17</sup>.

To mitigate these issues, compositional tuning by direct substitution of Br with other types of anion has been identified as one of the most effective strategies. Chlorine (Cl) has been the most extensively studied because of its classification in the same group as I and Br (refs. 18–20). A previous study successfully integrated Cl into a perovskite lattice, reducing the  $V_{\text{oc}}$  loss by 100 mV in a 1.67-eV wide-bandgap perovskite<sup>18</sup>. Furthermore, the pseudohalide thiocyanate ( $\text{SCN}^-$ ) has recently garnered interest because it can affect the crystallization process of perovskite films when used as an additive<sup>21</sup>. However, solid-state nuclear magnetic resonance characterization indicates that  $\text{SCN}^-$  does not successfully substitute for halides to create a stable three-dimensional perovskite lattice<sup>22,23</sup>. Few of these approaches have been successful in producing UWBG perovskites with bandgaps exceeding 1.90 eV. The achievement of high-efficiency top subcells remains an important hurdle in realizing the projected high efficiency of TJSCs.

In our work, we successfully incorporated a previously unknown pseudohalide, cyanate ( $\text{OCN}^-$ ), into UWBG perovskites. Cyanate exhibits an effective ionic radius (1.97 Å) comparable to that of bromide (1.95 Å). Although various studies have suggested the potential of incorporating OCN into the perovskite, until now, there has been no experimental evidence to confirm the successful integration of OCN into the perovskite lattice<sup>24–26</sup>. Using atomic-resolution transmission electron microscopy (TEM) and electron energy loss spectroscopy, we confirmed the successful integration of OCN ions into the perovskite lattice. This substitution led to lattice constant reduction, bandgap increment and enhanced crystal orientation.

<sup>1</sup>Department of Chemical and Biomolecular Engineering, National University of Singapore, Singapore, Singapore. <sup>2</sup>Solar Energy Research Institute of Singapore (SERIS), National University of Singapore, Singapore, Singapore. <sup>3</sup>Beijing Key Laboratory of Microstructure and Properties of Solids, Faculty of Materials and Manufacturing, Beijing University of Technology, Beijing, People's Republic of China. <sup>4</sup>Suzhou Maxwell Technologies, Suzhou, People's Republic of China. <sup>5</sup>TUM School of Natural Sciences, Department of Physics, Chair for Functional Materials, Technical University of Munich, Garching, Germany. <sup>6</sup>Heinz Maier-Leibniz Zentrum (MLZ), Technical University of Munich, Garching, Germany. <sup>7</sup>These authors contributed equally: Shunchang Liu, Yue Lu. <sup>✉</sup>e-mail: yi.hou@nus.edu.sg

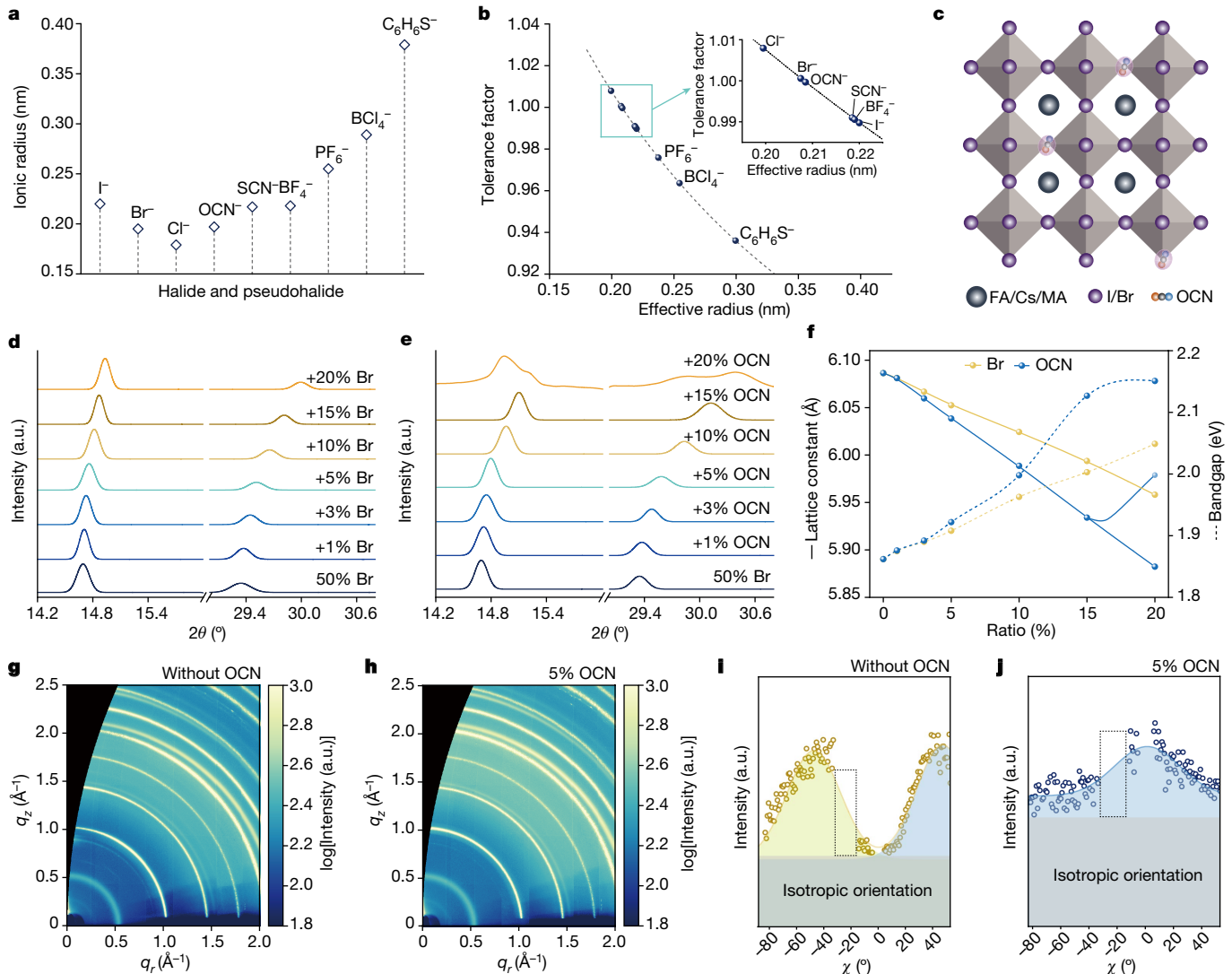


**Fig. 1 | Characterization of OCN-substituted perovskite film.** **a**, Effective ionic radius of halides and pseudohalides. **b**, Tolerance factor of 5%-pseudohalide-substituted perovskite  $\text{FA}_{0.75}\text{Cs}_{0.25}\text{Pb}(\text{I}_{0.5}\text{Br}_{0.5})_3$ . **c**, Schematic of the crystal lattice of OCN-substituted perovskite. **d,e**, XRD spectra of (001) and (002) peaks of the perovskite with various concentrations of Br and OCN replacing I. **f**, Lattice constant calculated from **d** and **e** and corresponding bandgap

calculated from the ultraviolet-visible spectra shown in Supplementary Fig. 3. **g,h**, 2D GIWAXS data transferred to  $q$ -space of the perovskite without (**g**) and with (**h**) 5% OCN. **i,j**, Perovskite orientation extracted from the (001) Bragg peak of without (**i**) and with (**j**) 5% OCN. The dashed box area is the detection gap of equipment. a.u., arbitrary units.

Furthermore, this incorporation induced moderate lattice distortion, contributing to increased film uniformity and elevated formation energy for defects. Consequently, a remarkable  $V_{\text{oc}}$  of 1.422 V was attained in OCN-substituted inverted UWBG perovskite solar cells, coupled with a  $V_{\text{oc}} \times \text{FF}$  (fill factor) product exceeding 80% of the Shockley–Queisser limit and stable performance under maximum power point (MPP) tracking. The cyanate-substituted perovskite was further implemented in a perovskite/perovskite/Si TJSC, achieving a certified efficiency of 27.10%, with a peak efficiency of 27.62%, across an active area of 1 cm<sup>2</sup>.

OCN serves as a linear pseudohalide that is anticipated to exhibit strong interaction with Pb. It possesses an effective ionic radius closely similar to that of Br, as evidenced in Fig. 1a and Supplementary Table 1. The tolerance factors for incorporating 5% pseudohalides into an UWBG perovskite were calculated for the  $\text{FA}_{0.75}\text{Cs}_{0.25}\text{Pb}(\text{I}_{0.5}\text{Br}_{0.5})_3$  perovskite and are presented in Fig. 1b. Among the studied pseudohalides, OCN demonstrates a tolerance factor most closely aligned with that of Br, making it a promising candidate for bromide substitution in UWBG perovskites, as depicted in Fig. 1c.

We incrementally increased the OCN concentration in  $\text{FA}_{0.75}\text{Cs}_{0.25}\text{Pb}(\text{I}_{0.5}\text{Br}_{0.5})_3$  perovskites while maintaining a consistent 50% Br concentration across various levels of OCN incorporation (0%, 1%, 3%, 5%, 10%, 15% and 20%). All prepared precursor solutions exhibit clear and transparent characteristics with a light-yellow hue, exhibiting no discernible variations, as evidenced in Supplementary Fig. 1. Perovskite films fabricated by the spin-coating technique demonstrate increasing transparency as the OCN concentration increases (Supplementary Fig. 2).

Based on X-ray diffraction (XRD) data, shown in Fig. 1d,e, we observe that similar to iodine substitution with bromine, the inclusion of OCN shifts the XRD peaks of the UWBG perovskite to higher angles. This provides evidence that OCN can be successfully integrated into the UWBG perovskite lattice structure. Interestingly, the lattice constant of perovskite films incorporating OCN is smaller than that of those films incorporating Br, as shown in Fig. 1f. This more pronounced ability of OCN to contract the lattice constant may signal alterations in the crystal structure. Specifically, on reaching an OCN concentration of 20%, bifurcated XRD peaks are detected, suggesting the emergence of dual phases in the perovskite film.

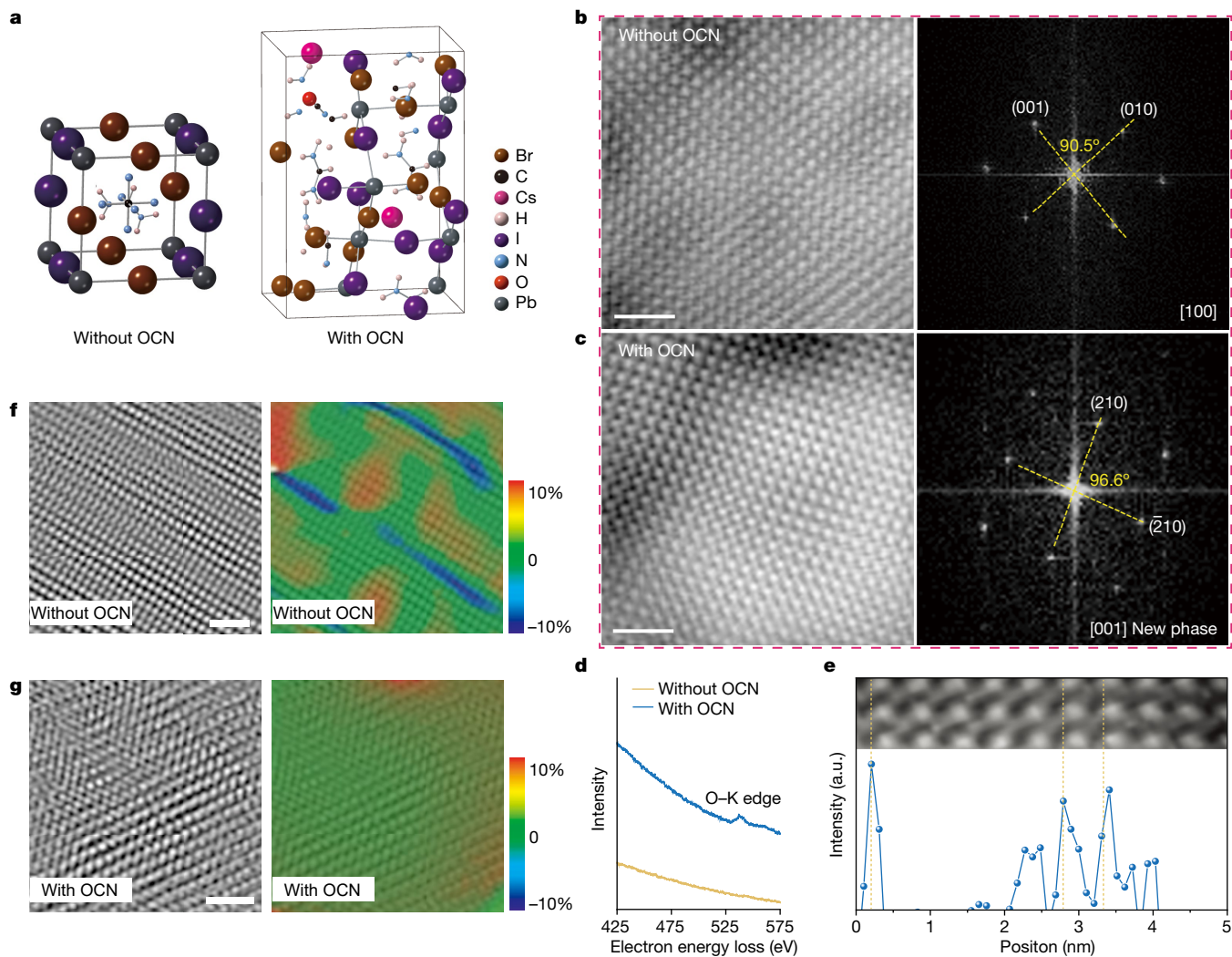


**Fig. 2 | TEM characterization of perovskite films.** **a**, The calculated crystal structure of perovskite without OCN and with 5% OCN. **b,c**, High-angle annular dark-field scanning transmission electron microscopy (HAADF-STEM) images of the perovskite films without and with 5% OCN, the corresponding FFT images are shown on the right side. **d**, EELS of the O-K edge of perovskite films without

or with 5% OCN. **e**, Atomic-resolution line scan for the EELS distribution of the O-K edge; we find that the oxygen atom is occupied at the side of the Pb atomic columns, which is consistent with the structure model in Supplementary Fig. 7. **f,g**, Distribution of the microstrain in perovskite films without (**f**) and with (**g**) 5% OCN. Scale bars, 2 nm (**b,c,f,g**).

Ultraviolet-visible absorption spectra, presented in Supplementary Fig. 3, corroborate these observations, revealing a consistent blueshift with increasing concentrations of both OCN and Br. Consistent with the XRD data, the optical bandgap shift of OCN-incorporated perovskites is more pronounced than that of Br-incorporated samples, with anomalous behaviour observed at a 20% OCN concentration (Fig. 1f).

To investigate the influence of OCN on the crystal structure orientation, we used grazing-incidence wide-angle X-ray scattering (GIWAXS)<sup>27</sup>. We selected a representative 5% OCN concentration for comparative analysis with OCN-free samples, as shown in Fig. 1g,h, as well as Supplementary Fig. 4. The line profiles, provided in Supplementary Fig. 5, validate the XRD findings by confirming the absence of the  $\delta$ -phase and thereby ensuring the phase purity of the samples. In the absence of OCN, the (001) Bragg peak of perovskite film predominantly exhibits a corner-up orientation, accompanied by weaker signals at  $0^\circ$  and  $90^\circ$ , as seen in Fig. 1i. By contrast, the OCN-substituted perovskite shows a strong diffraction intensity at  $0^\circ$ , as depicted in Fig. 1j, suggesting a more pronounced out-of-plane (face-on) orientation. This face-on orientation has previously been reported to enhance the charge-carrier transport efficiency in the material<sup>28</sup>.

To gain deeper insights into the impact of OCN on modifying the crystal lattice structure of perovskites, we performed first-principles calculations, as shown in Fig. 2a. These calculations show a subtle distortion of the Pb-X octahedral arrangement, which is further elaborated in Supplementary Table 2. Moreover, we used low-dose atomic-resolution TEM to systematically investigate the role of OCN in the perovskite lattice. TEM images, acquired along the [001] zone axis and presented in Fig. 2b and c and Supplementary Fig. 6, enabled us to obtain the corresponding fast Fourier transform (FFT) patterns for the perovskite films, both with and without OCN (Fig. 2a).

Our analysis shows that the angle between the (001) and (010) crystal planes of the original perovskite is approximately  $90.5^\circ$ , signifying a cubic phase with no evident structural distortion (Fig. 2b). However, on incorporating 5% OCN, a noticeable alteration in the angle in the diffraction patterns is observed, with an increase to  $96.6^\circ$  (Fig. 2c). This deviation is consistent with the calculated angle between the (210) and (−210) planes in the new OCN-incorporated phase. The shift in the angle can be primarily attributed to the induced structural distortion and changes in the vibrational degrees of freedom in the  $\text{Pb}_X_6$  octahedra<sup>29</sup>.

To elucidate the atomic placement of OCN in the new perovskite lattice, we used electron energy loss spectroscopy (EELS). As indicated

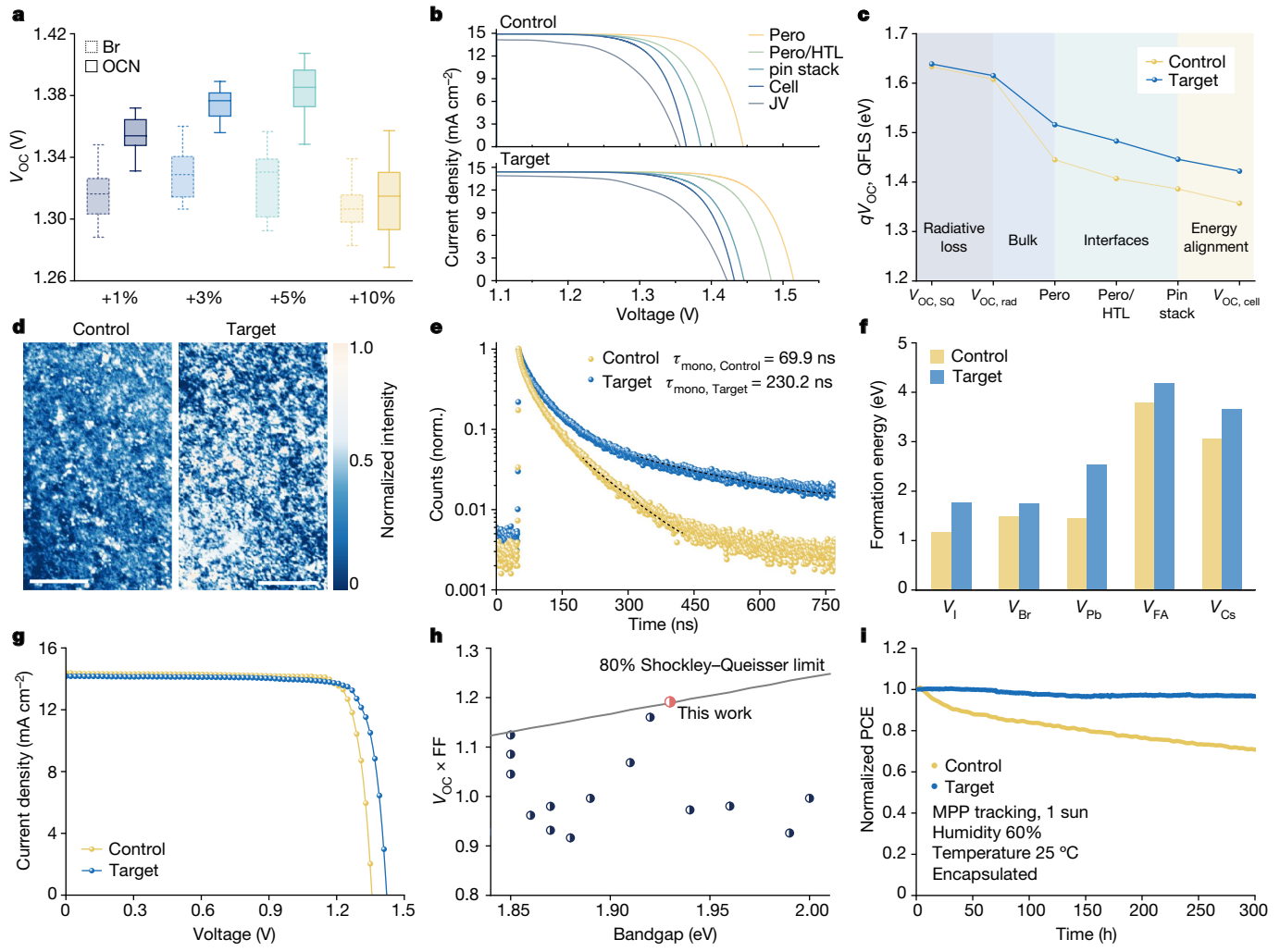


**Fig. 3 | Single-junction device  $V_{oc}$  loss analysis and device performance.**

**a**,  $V_{oc}$  comparison of different concentrations of Br and OCN. **b**, Pseudo- $J-V$  curves of control and target samples. **c**, Schematic of the voltage evolution with different stacks. **d**, Confocal photoluminescence mapping images of control and target films. Scale bars, 10  $\mu\text{m}$ . **e**, TRPL decays of control and target films.

**f**, Calculated formation energy of different vacancy defects. **g**,  $J-V$  curves of champion control and target single-junction devices. **h**, Comparison of  $V_{oc} \times FF$  products between this work and other reported UWBG perovskite solar cells with a p-i-n structure. **i**, Long-term operational stability under 1-sun illumination.

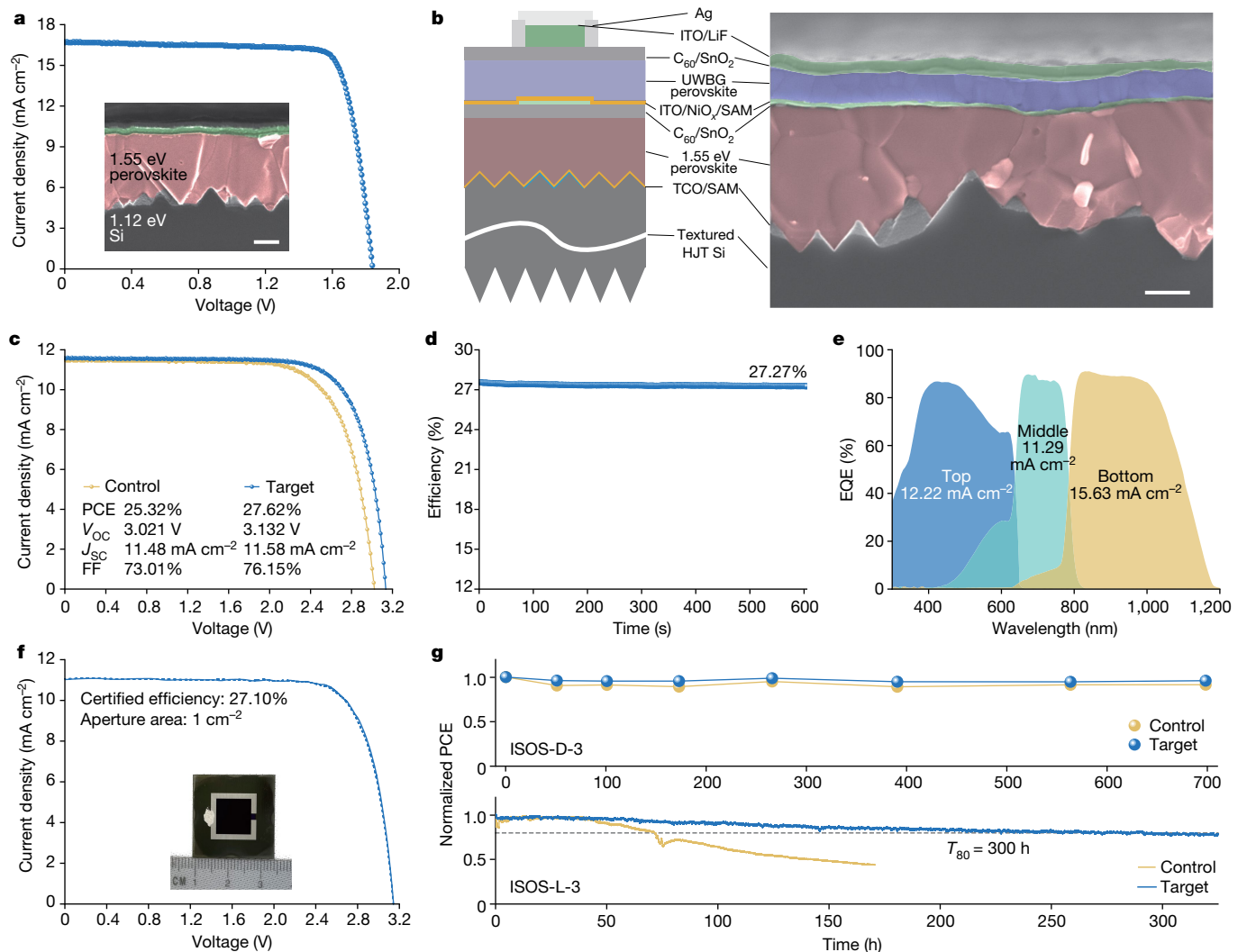
in our structural model and corroborated by Supplementary Fig. 7, OCN predominantly resides near the Pb columns when viewed from the [001] direction. Experimentally, the O-K-edge signal is readily apparent in EELS scans of OCN-substituted perovskites but absent in original films (Fig. 2d). Moreover, EELS high-resolution scans (Fig. 2e and Supplementary Fig. 8) indicate that the O-K-edge signal sporadically appears in the crystal lattice of the grains adjacent to atomic Pb columns. These observations confirm that OCN ions are randomly but consistently situated near Pb atoms, and consequently, O is bonded to Pb. All these findings are in line with our first-principles calculations, suggesting that OCN occupies the halide sites in the perovskite lattice, coupled with a slight distortion of the Pb-X octahedra (Fig. 2a and Supplementary Fig. 7).

The UWBG perovskite suffers from intrinsic inhomogeneity of halides, originating from the high Br fraction affecting the perovskite formation dynamics. Energy-dispersive X-ray spectroscopy (EDX) mapping (Supplementary Fig. 9) shows inhomogeneous I and Br distributions in original films, a problem rectified by OCN incorporation, which leads to more homogeneously distributed I and Br. We posit that OCN regulates the crystallization process, ensuring the simultaneous incorporation of both I and Br into the lattice<sup>30</sup>. High-resolution TEM further supports this claim, showing that OCN incorporation minimizes

microstrain inhomogeneities in the perovskite films (Fig. 2f,g and Supplementary Fig. 10).

Turning our attention to device performance, we assessed the  $V_{oc}$  evolution in UWBG perovskite solar cells with various OCN concentrations. OCN incorporation elevates  $V_{oc}$  beyond those values achievable with Br, peaking at 1.40 V with a 5% OCN concentration (Fig. 3a). The dramatic drop in  $V_{oc}$  of 10% OCN indicates that phase segregation has already begun because of large octahedral distortion, similar to with Cl. This result demonstrates that OCN shows excellent potential to reduce the  $V_{oc}$  loss in UWBG perovskite solar cells. Therefore, a perovskite with 5% OCN content ( $\text{FA}_{0.60}\text{MA}_{0.15}\text{Cs}_{0.25}\text{Pb}(\text{I}_{0.45}\text{Br}_{0.5}\text{OCN}_{0.05})_3$ ) was selected as the target for device investigation, whereas a perovskite ( $\text{FA}_{0.60}\text{MA}_{0.15}\text{Cs}_{0.25}\text{Pb}(\text{I}_{0.43}\text{Br}_{0.57})_3$ ) with a comparable bandgap was used as the control (Supplementary Fig. 11).

Our investigation commenced with intensity-dependent photoluminescence measurements, and the corresponding quasi-Fermi-level splitting values (QFLSs) were calculated in relation to various light intensities for distinct device configurations (Supplementary Fig. 12). We subsequently plotted pseudo- $J-V$  curves derived from these QFLSs, alongside  $J-V$  curves from standard cells, for both control and target devices<sup>31,32</sup> (Fig. 3b). Although the addition of transport layers leads to a decline in the pseudo-photovoltaic performance across

**Fig. 4 | Device characteristics of dual-junction solar cell and TJSCs.**

**a**,  $J-V$  curve from the reverse scan of champion dual-junction device. Inset, cross-sectional SEM image of the typical dual-junction device. **b**, Schematic structure and cross-sectional SEM image of the TJSC. Ag is deposited as a metal frame, which is not presented in the SEM image. **c**,  $J-V$  curves of control and target TJSCs. **d**, MPP tracking measurement of the champion TJSC. **e**, EQE

spectra for each subcell of the champion TJSC. **f**, Certified  $J-V$  curves by SIMIT. Solid line, reverse scan; dashed line, forward scan. Inset, picture of the champion device. **g**, Long-term stability test of control and target TJSCs following ISOS-D-3 and ISOS-L-3 protocols. In the ISOS-D-3 test, the initial PCEs of the control and target devices are 21.9% and 25.7%. In the ISOS-L-3 test, the initial PCEs of the control and target devices are 22.2% and 25.3%. Scale bars, 500 nm (**a,b**).

all samples, the target devices consistently outperform their control counterparts.

To further quantify voltage losses, we used high-resolution external quantum efficiency (EQE) measurements and calculated the radiative voltage limits for both control and target devices (Supplementary Fig. 13 and Supplementary Table 3). A summary of the device  $V_{OC}$ , QFLS, radiative voltage ( $V_{OC,rad}$ ), and Shockley–Queisser limit ( $V_{OC,SQ}$ ) is presented in Fig. 3c and Supplementary Table 3. Although both the control and target stacks exhibit similar levels of non-radiative loss at each interface, they significantly differ in their bulk non-radiative losses. Specifically, the bulk non-radiative loss of the target sample is reduced by 71 mV, underscoring its ability to mitigate non-radiative recombination defects in the bulk of perovskites.

Further supporting this, confocal photoluminescence images and steady-state photoluminescence data (Fig. 3d and Supplementary Fig. 14) show heightened and more uniform emission intensity for the target samples. This points to a reduction in non-radiative recombination defects in the OCN-original films. Moreover, time-resolved photoluminescence (TRPL) studies show a markedly slower decay

rate for the target sample (Fig. 3e). These observations collectively suggest suppression of bulk non-radiative recombination pathways in the target sample<sup>33</sup>. Density functional theory calculations confirm that incorporation of OCN increases the defect formation energy and the energy barrier of ion migration (Fig. 3f and Supplementary Fig. 15). These experimental and calculation results collectively affirm that the incorporation of OCN into perovskite lattice can effectively reduce the concentration of mobile ions (Supplementary Fig. 16) as well as defects<sup>34–36</sup>, which would be beneficial for the perovskite stability and device performance.

With these improvements, we examined the best-performing single-junction solar cell with a p-i-n structure (glass/indium tin oxide (ITO)/nickel oxide ( $NiO_x$ )/[4-(3,6-dimethyl-9H-carbazol-9-yl)butyl] phosphonic acid (Me-4PACz)/perovskite/PCBM/BCP/Ag). As shown in Fig. 3g and Supplementary Table 4, the incorporation of OCN sharply increases  $V_{OC}$  from 1.357 V to 1.422 V, agreeing well with the above analysis (Supplementary Fig. 17). We conducted a comparison of  $V_{OC} \times FF$  products among our work and previously reported UWBG perovskite solar cells with p-i-n structures, which are well suited for top cells

in TJSCs. Our target device delivers a  $V_{OC} \times FF$  product of 80.3% of its Shockley–Queisser limit, surpassing all the reported results (Fig. 3h). This  $V_{OC} \times FF$  product makes it promising as a top cell in TJSCs. Finally, when continuously operated under the MPP for 300 h with encapsulation in air (relative humidity > 60%), the PCE of the target device remains above 96%, whereas the control device preserves approximately 70% PCE (Fig. 3i).

Encouraged by the good homogeneity and promising device performance imparted by OCN, we fabricated perovskite/perovskite/Si TJSCs. Before assembling a TJSC, an outstanding perovskite (middle cell)–Si dual-junction half-cell must be obtained. A small-textured silicon heterojunction solar cell, based on a 130- $\mu\text{m}$ -thick n-type Czochralski Si wafer (Supplementary Fig. 18), was used as the bottom cell, and a perovskite,  $\text{FA}_{0.9}\text{Cs}_{0.1}\text{PbI}_3$  with a 1.55-eV bandgap, was chosen as the middle cell to balance the excellent performance and decent short-circuit current density ( $J_{SC}$ ). This 1.55 eV perovskite middle cell exhibits commendable performance in single-junction devices, regardless of pixel area or large area scale<sup>37</sup> (Supplementary Fig. 19). Figure 4a shows a cross-section scanning electron microscopy (SEM) image of this dual-junction device with a stack of textured Si/ITO/Me-4PACz/1.55-eV perovskite/C<sub>60</sub>/SnO<sub>x</sub>/ITO/LiF. The perovskite film is uniformly deposited on textured Si with a thickness of approximately 1.3  $\mu\text{m}$  to harvest as much light as possible. Consequently, a 25.03% PCE is obtained from the reverse scan, with a  $V_{OC}$  of 1.841 V,  $aJ_{SC}$  of 16.71 mA cm<sup>-2</sup> and an FF of 81.3%, whereas the PCE from the forward scan is 24.42% (with an aperture area of about 1 cm<sup>2</sup>) (Fig. 4a and Supplementary Fig. 20). The integrated  $J_{SC}$  values from the corresponding EQE for the top cell and bottom cell are 23.85 mA cm<sup>-2</sup> and 16.05 mA cm<sup>-2</sup>, respectively (Supplementary Fig. 21). This current mismatch is expected because of the unmatched bandgaps.

The smooth top surface and robust performance of the dual-junction half-cell create an ideal substrate for the subsequent deposition of UWBG perovskites. We integrated the UWBG perovskite with this dual-junction half-cell to create a monolithic perovskite/perovskite/Si TJSC. The final configuration of this TJSC is textured Si/ITO/Me-4PACz/1.55-eV perovskite/C<sub>60</sub>/SnO<sub>x</sub>/ITO/NiO<sub>x</sub>/Me-4PACz/UWBG perovskite/C<sub>60</sub>/SnO<sub>x</sub>/ITO/LiF, as shown in Fig. 4b and Supplementary Fig. 22. The cross-sectional SEM image shows that the UWBG perovskite uniformly covers the middle cell without obvious damage to the underneath layer. EDX mapping of key elements was conducted to provide additional insight into the structural integrity of the device. As shown in Supplementary Fig. 23, distinct boundaries between elements corresponding to different layers are visible, and no signs of elemental diffusion are evident. These SEM and EDX analyses confirm that despite the complexity of this TJSC, each layer is meticulously arranged in sequence, without any dissolution or degradation between the layers. Figure 4c and Supplementary Fig. 24 show the  $J-V$  curves of the perovskite/perovskite/Si TJSCs with different top cells. Notably, the incorporation of OCN boosts the efficiency from 25.32% ( $V_{OC} = 3.021$  V,  $J_{SC} = 11.48$  mA cm<sup>-2</sup>, FF = 73.01%) to 27.62% ( $V_{OC} = 3.132$  V,  $J_{SC} = 11.58$  mA cm<sup>-2</sup>, FF = 76.15%) with an active area of about 1 cm<sup>2</sup>. The statistical results also show that target devices give narrower performance parameter distributions (Supplementary Fig. 25). After continuous operation under MPP tracking for 600 s, the efficiency of the champion device stabilizes at 27.27% (Fig. 4d and Supplementary Fig. 26). The integrated  $J_{SC}$  values from EQE measurements for the top, middle and bottom cells of the champion target device are 12.22 mA cm<sup>-2</sup>, 11.29 mA cm<sup>-2</sup> and 15.63 mA cm<sup>-2</sup>, respectively (Fig. 4e), aligned with the  $J-V$  curve. We also sent the champion device to an accredited independent PV calibration laboratory (Shanghai Institute of Microsystem and Information Technology, SIMIT) for certification, and a certified PCE of 27.10% was obtained under reverse scan with no hysteresis (Fig. 4f and Supplementary Fig. 27), agreeing well with the value measured in-house. Our result represents the highest-performing perovskite-based TJSC to date, as substantiated by Supplementary Fig. 28 and Supplementary Table 5.

We evaluated the long-term stability of TJSCs using International Summit on Organic Photovoltaic Stability (ISOS) protocols, ISOS-D-3 and ISOS-L-3 (Fig. 4g). After 700 h of exposure to a temperature of 65 °C and 85% relative humidity, the encapsulated control and target devices retained 91% and 96% of their initial PCEs, respectively. Furthermore, under AM 1.5 G 1-sun illumination at 65 °C and 50% relative humidity, the target device maintained 80% of the original PCE after 300 h ( $T_{80} = 300$  h), whereas the control device quickly dropped to 80% of the initial PCE after 70 h.

In conclusion, we discover that the pseudohalide OCN<sup>-</sup>, which bears a similar effective ionic radius to Br<sup>-</sup> but has been comparatively understudied, can be integrated into the crystal lattice of UWBG perovskites. Comprehensive TEM analyses show that the linear OCN ion assumes a fixed orientation in the lattice and induces a minor distortion of the PbX<sub>6</sub> octahedron. This substitution not only enhances the uniformity of the perovskite film but also elevates the formation energy of vacancy defects. Consequently, the introduction of OCN elevates  $V_{OC}$  from 1.357 V to 1.422 V and results in the highest  $V_{OC} \times FF$  product for UWBG perovskite solar cells. Our findings on the role of the pseudo-halide OCN ion contribute a fresh perspective to understanding how halide anions influence perovskite properties. Moreover, we engineered monolithic perovskite/perovskite/Si TJSCs using commercial heterojunction Si solar cells and achieved an efficiency of 27.62%, certified at 27.10%, highlighting the potential of perovskite-based TJSCs. Finally, we rigorously studied the long-term stability of the TJSCs following ISOS-D-3 and ISOS-L-3 protocols.

## Online content

Any methods, additional references, Nature Portfolio reporting summaries, source data, extended data, supplementary information, acknowledgements, peer review information; details of author contributions and competing interests; and statements of data and code availability are available at <https://doi.org/10.1038/s41586-024-07226-1>.

- Yeom, K. M., Kim, S. U., Woo, M. Y., Noh, J. H. & Im, S. H. Recent progress in metal halide perovskite-based tandem solar cells. *Adv. Mater.* **32**, 2002228 (2020).
- Li, H. & Zhang, W. Perovskite tandem solar cells: from fundamentals to commercial deployment. *Chem. Rev.* **120**, 9835–9950 (2020).
- Xu, F., Zhang, M., Li, Z., Yang, X. & Zhu, R. Challenges and perspectives toward future wide-bandgap mixed-halide perovskite photovoltaics. *Adv. Energy Mater.* **13**, 2203911 (2023).
- Zhou, Y., Poli, I., Meggiolaro, D., De Angelis, F. & Petrozza, A. Defect activity in metal halide perovskites with wide and narrow bandgap. *Nat. Rev. Mater.* **6**, 986–1002 (2021).
- Caprioglio, P. et al. Open-circuit and short-circuit loss management in wide-gap perovskite p-i-n solar cells. *Nat. Commun.* **14**, 932 (2023).
- Leijtens, T., Bush, K. A., Prasanna, R. & McGehee, M. D. Opportunities and challenges for tandem solar cells using metal halide perovskite semiconductors. *Nat. Energy* **3**, 828–838 (2018).
- Hörantner, M. T. et al. The potential of multijunction perovskite solar cells. *ACS Energy Lett.* **2**, 2506–2513 (2017).
- Mariotti, S. et al. Interface engineering for high-performance, triple-halide perovskite–silicon tandem solar cells. *Science* **381**, 63–69 (2023).
- Lin, R. et al. All-perovskite tandem solar cells with 3D/3D bilayer perovskite heterojunction. *Nature* **620**, 994–1000 (2023).
- Zhu, J. et al. A donor–acceptor-type hole-selective contact reducing non-radiative recombination losses in both subcells towards efficient all-perovskite tandems. *Nat. Energy* **8**, 714–724 (2023).
- Wen, J. et al. Steric engineering enables efficient and photostable wide-bandgap perovskites for all-perovskite tandem solar cells. *Adv. Mater.* **34**, 2110356 (2022).
- Best research-cell efficiency chart. NREL <https://www.nrel.gov/pv/cell-efficiency.html> (2023).
- Ho-Baillie, A. W. Y. et al. Recent progress and future prospects of perovskite tandem solar cells. *Appl. Phys. Rev.* **8**, 041307 (2021).
- Wang, Z. et al. Suppressed phase segregation for triple-junction perovskite solar cells. *Nature* **618**, 74–79 (2023).
- Choi, Y. J., Lim, S. Y., Park, J. H., Ji, S. G. & Kim, J. Y. Atomic layer deposition-free monolithic perovskite/perovskite/silicon triple-junction solar cells. *ACS Energy Lett.* **8**, 3141–3146 (2023).
- Yin, W.-J., Shi, T. & Yan, Y. Unique properties of halide perovskites as possible origins of the superior solar cell performance. *Adv. Mater.* **26**, 4653–4658 (2014).
- Hoke, E. T. et al. Reversible photo-induced trap formation in mixed-halide hybrid perovskites for photovoltaics. *Chem. Sci.* **6**, 613–617 (2015).
- Xu, J. et al. Triple-halide wide-band gap perovskites with suppressed phase segregation for efficient tandems. *Science* **367**, 1097–1104 (2020).

19. Jang, D. M. et al. Reversible halide exchange reaction of organometal trihalide perovskite colloidal nanocrystals for full-range band gap tuning. *Nano Lett.* **15**, 5191–5199 (2015).
20. Liang, P.-W. et al. High-performance planar-heterojunction solar cells based on ternary halide large-band-gap perovskites. *Adv. Energy Mater.* **5**, 1400960 (2015).
21. Lin, P.-Y. et al. Pseudo-halide perovskite solar cells. *Adv. Energy Mater.* **11**, 2100818 (2021).
22. Saparov, B. & Mitzi, D. B. Organic–inorganic perovskites: structural versatility for functional materials design. *Chem. Rev.* **116**, 4558–4596 (2016).
23. Lu, H. et al. Vapor-assisted deposition of highly efficient, stable black-phase FAPbI<sub>3</sub> perovskite solar cells. *Science* **370**, eabb8985 (2020).
24. Xu, Z., Chen, M. & Liu, S. Pseudo-halide induced tunable electronic and excitonic properties in two-dimensional single-layer perovskite for photovoltaics and photoelectronic applications. *J. Energy Chem.* **36**, 106–113 (2019).
25. Li, J. et al. Linear pseudo-halogen anion passivating defects for MAPbI<sub>3</sub> perovskite solar cells. *Phys. B Condens. Matter* **651**, 414591 (2023).
26. Tao, J. et al. Additive engineering for efficient and stable MAPbI<sub>3</sub>-perovskite solar cells with an efficiency of over 21%. *ACS Appl. Mater. Interfaces* **13**, 44451–44459 (2021).
27. Schlipf, J. & Müller-Buschbaum, P. Structure of organometal halide perovskite films as determined with grazing-incidence X-ray scattering methods. *Adv. Energy Mater.* **7**, 1700131 (2017).
28. Zheng, X. et al. Managing grains and interfaces via ligand anchoring enables 22.3%-efficiency inverted perovskite solar cells. *Nat. Energy* **5**, 131–140 (2020).
29. Wei, W. et al. An unusual phase transition driven by vibrational entropy changes in a hybrid organic-inorganic perovskite. *Angew. Chem. Int. Ed.* **57**, 8932–8936 (2018).
30. Huang, T. et al. Performance-limiting formation dynamics in mixed-halide perovskites. *Sci. Adv.* **7**, eabj1799 (2021).
31. Tian, J. et al. Quantifying the energy losses in CsPbI<sub>2</sub>Br perovskite solar cells with an open-circuit voltage of up to 1.45 V. *ACS Energy Lett.* **7**, 4071–4080 (2022).
32. Stolterfoht, M. et al. How to quantify the efficiency potential of neat perovskite films: perovskite semiconductors with an implied efficiency exceeding 28%. *Adv. Mater.* **32**, 2000080 (2020).
33. Peng, W. et al. Reducing nonradiative recombination in perovskite solar cells with a porous insulator contact. *Science* **379**, 683–690 (2023).
34. Zhang, Y. et al. Improved fatigue behaviour of perovskite solar cells with an interfacial starch-polyiodide buffer layer. *Nat. Photon.* **17**, 1066–1073 (2023).
35. Deng, Y. et al. Defect compensation in formamidinium–caesium perovskites for highly efficient solar mini-modules with improved photostability. *Nat. Energy* **6**, 633–641 (2021).
36. Game, O. S. et al. Ions matter: description of the anomalous electronic behavior in methylammonium lead halide perovskite devices. *Adv. Funct. Mater.* **27**, 1606584 (2017).
37. Bu, T. et al. Lead halide-templated crystallization of methylamine-free perovskite for efficient photovoltaic modules. *Science* **372**, 1327–1332 (2021).

**Publisher's note** Springer Nature remains neutral with regard to jurisdictional claims in published maps and institutional affiliations.

Springer Nature or its licensor (e.g. a society or other partner) holds exclusive rights to this article under a publishing agreement with the author(s) or other rightsholder(s); author self-archiving of the accepted manuscript version of this article is solely governed by the terms of such publishing agreement and applicable law.

© The Author(s), under exclusive licence to Springer Nature Limited 2024

## Methods

### Materials

Caesium iodide (CsI, 99.99%), methyl acetate (anhydrous), chlorobenzene (CB, anhydrous), dimethylformamide (DMF, anhydrous) and dimethyl sulphoxide (DMSO, anhydrous) were purchased from Sigma-Aldrich. Formamidinium iodide (FAI) and methylammonium cyanate were purchased from Greatcell Solar Materials; lead iodide ( $PbI_2$ ), lead bromide and Me-4PACz were purchased from Tokyo Chemical Industry. Silver was purchased from Kurt J. Lesker. [6,6]-Phenyl-C<sub>61</sub>-butyric acid methyl ester (PCBM), C<sub>60</sub> and bathocuproine (BCP) were purchased from Lumtec. NiO<sub>x</sub> nanoparticles were synthesized based on our previous recipe<sup>38</sup>.

### Computational details

All the spin-polarized density functional theory calculation was performed using the plane-wave pseudopotential method based on the PBEsol exchange-correlation functional, which is implemented by the Vienna ab initio simulation package (v.5.4.4). The valence wave functions were expanded by plane wave with a cutoff energy of 400 eV. The  $1 \times 2 \times 1$  hybrid perovskite model was established to model the wide-bandgap perovskites used in the device ( $FA_{0.75}Cs_{0.25}Pb(I_{0.5}Br_{0.5})_3$ ). Then the OCN<sup>-</sup> was further introduced into the perovskite lattice by substituting one I<sup>-</sup>. The Brillouin zone was sampled using a  $3 \times 6 \times 4$  k points mesh for geometry optimization. All the structures were optimized until the force on each atom was less than  $0.02 \text{ eV } \text{\AA}^{-1}$ .

The vacancy formation energies of different species in the perovskites were calculated with the pure substance of corresponding elements as references—for example, I solid, Br solid and Pb metal. The calculation of I<sup>-</sup> vacancy formation energy is listed as an example according to the equation. Therefore, owing to the choices of different references, the absolute values of the calculated formation energies are incomparable with each other. We compared only the relative formation energies change for the same defects in OCN perovskites and original wide-bandgap perovskites.



### Device fabrication

**Silicon solar cells.** Silicon heterojunction bottom cells were fabricated on double-side textured c-Si wafers (CZ n-type Si (100), about  $1 \Omega \text{ cm}$  resistivity,  $150 \mu\text{m}$  thickness) in the R&D centre of Suzhou Maxwell Technologies. Detailed information can be found in our previous report<sup>39</sup>.

**Single-junction solar cells.** The ITO glass substrates were cleaned with detergent first, then ultrasonically washed with deionized water, acetone and isopropanol (IPA) for 20 min, respectively. After drying by N<sub>2</sub>, they were treated with ultraviolet ozone for 15 min. The substrates were spin-coated with NiO<sub>x</sub> nanoparticles ( $10 \text{ mg ml}^{-1}$  in water) at 4,000 rpm for 30 s, followed by heating at  $120^\circ\text{C}$  for 10 min in the air. Then the substrates were transferred to the nitrogen-filled glovebox. The Me-4PACz ( $1 \text{ mg ml}^{-1}$  in IPA) was spin-coated on the substrates at 4,000 rpm for 30 s and then heated at  $100^\circ\text{C}$  for 10 min. The 1 M perovskite ( $FA_{0.75}Cs_{0.25}Pb(I_{0.5}Br_{0.5})_3$ ) stock solution (1%  $PbI_2$  extra) contains 65 mg CsI, 129 mg FAI, 120 mg  $PbI_2$  and 275 mg  $PbBr_2$  that were dissolved in 1 ml mixed solvent of DMF:DMSO (v:v = 4:1). The perovskite precursor solution was shaken for about overnight at  $65^\circ\text{C}$  to make it fully dissolved and then used for preparing perovskite films. Different concentrations of OCN perovskite solution were prepared by the same method but an equivalent molar amount of MAOCN was used to replace FAI. The control perovskite ( $FA_{0.60}MA_{0.15}Cs_{0.25}Pb(I_{0.43}Br_{0.57})_3$ ) solution contains 65 mg CsI, 103 mg FAI, 17 mg MABr, 106 mg  $PbI_2$  and 286 mg  $PbBr_2$  that were dissolved using the same method. For the spin-coating process, the perovskite solution was spin-coated on the substrates at 4,000 rpm for 45 s with

an acceleration of 2,000 rpm per second and 200 ml methyl acetate was slowly dropped on the substrates at the last 15 s before the ending. The perovskite films were annealed at  $100^\circ\text{C}$  for 10 min. Then, PCBM ( $20 \text{ mg ml}^{-1}$  in CB) was spin-coated at 1,500 rpm for 30 s and annealed at  $100^\circ\text{C}$  for 5 min. BCP ( $2 \text{ mg ml}^{-1}$  in IPA) was dynamically spin-coated at 5,000 rpm for 20 s and then annealed at  $80^\circ\text{C}$  for 1 min. Finally, Ag (100 nm) was deposited to complete the device fabrication.

**Triple-junction solar cells.** The textured Si with 15 nm ITO was first treated with ultraviolet ozone for 5 min. The Me-4PACz ( $0.75 \text{ mg ml}^{-1}$  in IPA) was spin-coated on the Si at 4,000 rpm for 30 s in air, then the Si was immediately transferred to N<sub>2</sub>-glovebox and annealed for 10 min. The 1.55-eV perovskite solution was prepared based on our previous report. The 1.55-eV perovskite solution was spin-coated on the Si at 2,000 rpm for 20 s and 5,000 rpm for 30 s and N<sub>2</sub> gas was blown on top of the at the last 20 s. The perovskite film was pre-annealed at  $70^\circ\text{C}$  for 2 min in N<sub>2</sub>-glovebox and then annealed at  $150^\circ\text{C}$  for 8 min in air with 30% relative humidity. Then, C<sub>60</sub> (15 nm) was deposited by a thermal evaporator. Then, the following steps were taken: (1) For dual-junction solar cells, SnO<sub>2</sub> (20 nm) was deposited by an atomic-layer deposition system, then the samples were transferred to a magnetron sputtering system to deposit 60 nm ITO, and finally, a 500 nm Ag frame was deposited to complete the dual-junction device. (2) For TJSCs, the SnO<sub>2</sub> (25 nm) and ITO (8 nm) were deposited by the same method. Then the samples were transferred to a plasma machine for 5 s treatment with 350 W power. After that, the NiO<sub>x</sub> nanoparticles ( $25 \text{ mg ml}^{-1}$ , H<sub>2</sub>O:IPA = 3:1) were spin-coated at 4,000 rpm for 30 s, followed by annealing at  $120^\circ\text{C}$  for 3 min in air. The Me-4PACz ( $0.75 \text{ mg ml}^{-1}$  in IPA) was spin-coated at 4,000 rpm for 30 s. Then, the samples were transferred to N<sub>2</sub>-glovebox and annealed at  $100^\circ\text{C}$  for 3 min. The UWBG perovskite film was deposited as the single-junction device but was annealed only for 5 min. Finally, C<sub>60</sub> (15 nm)/SnO<sub>2</sub> (20 nm)/ITO (60 nm)/Ag frame (500 nm)/LiF (60 nm) were deposited sequentially by the same method.

### Material characterizations

SEM images were taken with Regulus SU8200 system (Hitachi) at 3 kV accelerating voltage under SE mode. The cross-sectional samples of perovskite solar cells and films used for TEM characterization were prepared by a focused ion beam-scanning electron microscopy double-beam system (FEI, Helios Nano Lab 600i), which includes an electron beam gun and a gallium ion beam gun. A voltage of 30 kV for the gallium ion beam was operated to slice the samples. Meanwhile, the electron beam was operated at 2 kV and the beam current was 0.17 nA. Furthermore, a protective Pt layer on the surface of the samples was fabricated using a gas deposition system to protect the damage to the perovskite samples. During the sample preparation, freezing the samples and a Nano-mill (Fischione company) operation are also needed. The TEM images (with HRTEM and HAADF-STEM models) were captured on the Titan-G2 (60–300) and JEOL ARM-300 spherical aberration correction transmission electron microscopes, which were operated at a voltage of 300 kV and equipped with the four silicon drift windowless detectors of X-ray energy dispersion spectrometer (Super-EDX). The energy resolution of Super-EDX was 137 eV and the energy resolution of the electron energy loss spectrum was 0.3 eV.

Absorbance and transmittance spectra were recorded with Agilent Cary 7000 spectrophotometer. XRD profiles were recorded on an X-ray diffractometer (D8, Bruker) with Cu K $\alpha$  radiation ( $\lambda = 0.1542 \text{ nm}$ ). XPS measurements were performed with the Kratos Axis Ultra XPS system. Steady-state photoluminescence and TRPL measurements were conducted by PicoQuant FluoTime 300 spectrometer with laser excitation at 515.8 nm in ambient air with the films encapsulated. Confocal photoluminescence mappings were measured on a Nikon A1 confocal microscope equipped with a 633-nm continuous-wave laser. Grazing-incidence wide-angle X-ray scattering experiments

# Article

were conducted at the PETRA III synchrotron P03 beamline at DESY, Hamburg<sup>40</sup>. A monochromatic X-ray beam with an energy of 11.7 keV and a beam size of  $23 \times 32 \mu\text{m}^2$  was used. The samples were probed at an incidence angle of 0.6° to study the sample structure. The sample-to-detector distance was calibrated by the CeO<sub>2</sub> sample. The images were collected by the Lamdba 7.5 M detector, and the obtained images were analysed by our INSIGHT software package. All samples were measured in an N<sub>2</sub>-filled closed chamber.

## Device characterization

*J–V* measurements of the single-junction device were recorded with a Keithley 2400 source meter under simulated 1-sun AM 1.5 G illumination (100 mW cm<sup>-2</sup>) in an N<sub>2</sub>-filled glovebox. The illumination area of the devices is defined by shadow masks of 0.05 cm<sup>2</sup>. *J–V* measurements of the dual-junction and triple-junction devices were recorded with SINUS-220, Wavelabs under simulated 1-sun AM 1.5 G illumination (100 mW cm<sup>-2</sup>) in air. The illumination area of the devices is defined by shadow masks of 1 cm<sup>2</sup>. MPP tracking of the single-junction devices was measured with MPP Tracking-4B system (Shenzhen Lancheng Technology) with LED simulated 1-sun intensity. The measurements were carried out in air at 25 °C with a relative humidity of about 60% with encapsulated devices. For the stability test of TJSCs, the devices were encapsulated between two glasses with butyl rubber edge sealant and polyolefin elastomer encapsulant, which were laminated in a laminator (EVG 501) at 100 °C for 10 min. Metal strips were used to extend the electrodes of the devices to the outside the glass. The MPP tracking measurements were performed using Solixon A-70, a Class A or better solar simulator dedicated to long-term irradiance exposure as per IEC 60904-9, with 1-sun AM 1.5 G illumination. EQE measurements were conducted using a Bentham PV-E300-IVT system. For the dual-junction device, the light bias from a halogen lamp with a 750-nm short-pass filter and a 850-nm long-pass filter was used to measure the spectral lines of the bottom and top subcells, respectively. For the triple-junction device, the light bias with 850 nm short-pass filter was used to measure the bottom subcell, the light bias with 800 nm long-pass filter and 650 nm short-pass filter was used to measure the middle subcell, and the light bias with 650 long-pass filter was used to measure the top subcell. For the high-resolution EQE, the light was chopped at 137 Hz and coupled into a Bentham monochromator. The resulting monochromatic light was focused onto the perovskite solar cell, and its current under short-circuit conditions was fed to a current preamplifier (Stanford SR 570) before it was analysed with a lock-in amplifier (Stanford SR830 DSP). The time constant of the lock-in amplifier was chosen to be 1 s, and the amplification of the preamplifier was increased to resolve low photocurrents. The EQE was determined by dividing the photocurrent of the cell by the flux of incoming photons, which was measured using a calibrated Si photodiode. Intensity-dependent photoluminescence measurements were conducted with an LP20-32 radiative efficiency meter (QYB). The laser (532 nm) was switched on 15 min before the measurement to allow it to

warm up and stabilize. The laser is then set to desired intensities and photoluminescence measurement is taken.

## Reporting summary

Further information on research design is available in the Nature Portfolio Reporting Summary linked to this article.

## Data availability

The data that support the findings of this study are available from the corresponding author upon request.

38. Chen, W. et al. Monolithic perovskite/organic tandem solar cells with 23.6% efficiency enabled by reduced voltage losses and optimized interconnecting layer. *Nat. Energy* **7**, 229–237 (2022).
39. Tang, T. et al. Achievement of 25.54% power conversion efficiency by optimization of current losses at the front side of silicon heterojunction solar cells. *Prog. Photovolt. Res. Appl.* **5**, 449–460 (2023).
40. Buffet, A. et al. P03, the microfocus and nanofocus X-ray scattering (MiNaXS) beamline of the PETRA III storage ring: the microfocus endstation. *J. Synchrotron Radiat.* **19**, 647–653 (2012).

**Acknowledgements** Y.H. acknowledges support from the MOE Tier 2 grant (MOE-T2EP1012-0005), the Ministry of Education (Singapore) and the National University of Singapore Presidential Young Professorship (A-0009174-03-00 and A-0009174-02-00). This research is supported by the National Research Foundation, Singapore, and A\*STAR (Agency for Science, Technology and Research) under its LCERFI program award no. U2102d2002. Y.L. acknowledges support from the National Natural Science Foundation of China (grant nos. 12074016 and 12274009), Beijing Natural Science Foundation (Z210016) and the General Program of Science and Technology Development Project of Beijing Municipal Education Commission (KM202110005003), the Research and Development Project from the Shanxi-Zheda Institute of Advanced Materials and Chemical Engineering (2022SX-TD001). P.M.-B. acknowledges support from the Deutsche Forschungsgemeinschaft (DFG, German Research Foundation) under Excellence Strategy-EXC 2089/1-390776260 (e-conversion) of Germany and TUM.solar in the context of the Bavarian Collaborative Research Project Solar Technologies Go Hybrid (SolTech). The authors of this paper are affiliated with the Solar Energy Research Institute of Singapore (SERIS), a research institute at the National University of Singapore. SERIS is supported by the National University of Singapore, the National Research Foundation Singapore, the Energy Market Authority of Singapore and the Singapore Economic Development Board. The computational work for this article was entirely performed on the resources of the National Supercomputing Centre (NSCC), Singapore (<https://www.nscc.sg>). We thank M. Schwartzkopf, K. Sun, Z. Li and X. Jiang for the support of beamtime at the DESY P03 beamline.

**Author contributions** S.L. and Y.H. conceived the idea and designed the experiments. Y.H. directed and supervised the project. S.L. fabricated the single-junction and triple-junction solar cells. Y.L. and M.S. conducted the TEM measurements. J.L. and H.L. assisted with the middle cell fabrication. R.G. and P.M.-B. conducted the GIWAXS measurement. X.J. assisted with  $V_{oc}$  loss and photoluminescence analysis. X.G. assisted with confocal photoluminescence measurements. R.L. assisted with the defect formation energy calculation. Y.-D.W. and X.W. assisted with the SEM measurement. Q.Z. assisted with the solar cell characterizations. C.Y. and S.Y. conducted the fabrication of silicon solar cells. S.L., Y.L., R.G., X.J. and Y.H. analysed the data and wrote the paper. All authors read and commented on the paper.

**Competing interests** The authors declare no competing interests.

## Additional information

**Supplementary information** The online version contains supplementary material available at <https://doi.org/10.1038/s41586-024-07226-1>.

**Correspondence and requests for materials** should be addressed to Yi Hou.

**Peer review information** *Nature* thanks Hairen Tan and the other, anonymous, reviewer(s) for their contribution to the peer review of this work.

**Reprints and permissions information** is available at <http://www.nature.com/reprints>.

## Solar Cells Reporting Summary

Nature Research wishes to improve the reproducibility of the work that we publish. This form is intended for publication with all accepted papers reporting the characterization of photovoltaic devices and provides structure for consistency and transparency in reporting. Some list items might not apply to an individual manuscript, but all fields must be completed for clarity.

For further information on Nature Research policies, including our [data availability policy](#), see [Authors & Referees](#).

### ► Experimental design

#### Please check: are the following details reported in the manuscript?

##### 1. Dimensions

Area of the tested solar cells

 Yes  
 No
 

0.08125 cm<sup>2</sup> (single junction) and 1.21 cm<sup>2</sup> (triple junction).

Method used to determine the device area

 Yes  
 No
 

Corresponding shadow masks were used during electrode deposition.

##### 2. Current-voltage characterization

Current density-voltage (J-V) plots in both forward and backward direction

 Yes  
 No
 

We provide J-V plots in both forward and backward direction in Fig. 4f, and Supplementary Fig. 18, 19, 20 and 24.

Voltage scan conditions

*For instance: scan direction, speed, dwell times*

 Yes  
 No
 

See details in Method.

Test environment

*For instance: characterization temperature, in air or in glove box*

 Yes  
 No
 

See details in Method.

Protocol for preconditioning of the device before its characterization

 Yes  
 No
 

No preconditioning condition is used.

Stability of the J-V characteristic

*Verified with time evolution of the maximum power point or with the photocurrent at maximum power point; see ref. 7 for details.*

 Yes  
 No
 

We provided MPPT data in Fig. 4d and Supplementary Fig. 26.

##### 3. Hysteresis or any other unusual behaviour

Description of the unusual behaviour observed during the characterization

 Yes  
 No
 

Minor hysteresis was observed for devices.

Related experimental data

 Yes  
 No
 

Throughout main text and Supplementary Information.

##### 4. Efficiency

External quantum efficiency (EQE) or incident photons to current efficiency (IPCE)

 Yes  
 No
 

We provide EQE measurement in Fig. 4e & Supplementary Fig. 17 & Supplementary Fig. 21.

A comparison between the integrated response under the standard reference spectrum and the response measure under the simulator

 Yes  
 No
 

We compare the integrated  $J_{sc}$  with one from JV scan. The difference between the integrated  $J_{sc}$  from EQE and  $J_{sc}$  from JV scan is 2.5% in triple junction solar cells, which is within accuracy confidence of the measurements.

For tandem solar cells, the bias illumination and bias voltage used for each subcell

 Yes  
 No
 

See details in Method.

##### 5. Calibration

Light source and reference cell or sensor used for the characterization

 Yes  
 No
 

See details in Method.

Confirmation that the reference cell was calibrated and certified

 Yes  
 No
 

Our solar simulator was calibrated by Si reference cell.(certificated by Newport.)

Calculation of spectral mismatch between the reference cell and the devices under test

Yes  
 No

The champion devices were sent to do certification, the certified device spectra mismatch factor for each subcell can be found in Supplementary Fig. 27.

## 6. Mask/aperture

Size of the mask/aperture used during testing

Yes  
 No

Optical aperture masks (0.055 cm<sup>2</sup> and 1 cm<sup>2</sup>) were used.

Variation of the measured short-circuit current density with the mask/aperture area

Yes  
 No

No significant variations was observed.

## 7. Performance certification

Identity of the independent certification laboratory that confirmed the photovoltaic performance

Yes  
 No

We provide certification data in Fig. 4f and Supplementary Fig. 27.

A copy of any certificate(s)

*Provide in Supplementary Information*

Yes  
 No

We provide certificate in Supplementary Fig. 27.

## 8. Statistics

Number of solar cells tested

Yes  
 No

See details in Supplementary Fig. 25.

Statistical analysis of the device performance

Yes  
 No

We provide statistics in Supplementary Fig. 25.

## 9. Long-term stability analysis

Type of analysis, bias conditions and environmental conditions

*For instance: illumination type, temperature, atmosphere humidity, encapsulation method, preconditioning temperature*

Yes  
 No

We provided stability data in Fig. 3i and Fig. 4g